Swansea University
Prifysgol Abertawe

Cronfa
Setting Research Free

Cronfa - Swansea University Open Access Repository

_____

This is an author produced version of a paper published in:
Theoretical and Applied Fracture Mechanics

Cronfa URL for this paper:
http://cronfa.swan.ac.uk/Record/cronfa36757

_____

Paper:

Farukh, F., Zhao, L., Barnard, N., Whittaker, M. & McColvin, G. (2017). Computational modelling of full interaction
between crystal plasticity and oxygen diffusion at a crack tip. *Theoretical and Applied Fracture Mechanics*
http://dx.doi.org/10.1016/j.tafmec.2017.10.010

_____

http://www.swansea.ac.uk/library/researchsupport/ris-support/

Computational modelling of full interaction between crystal plasticity and oxygen diffusion at a crack tip

F. Farukh[a], L.G. Zhao[b,*], N.C. Barnard[c], M.T. Whittaker[c], G. McColvin[d]

[a] School of Engineering and Sustainable Development, Faculty of Technology, De Montfort University, UK
[b] Wolfson School of Mechanical, Electrical and Manufacturing Engineering, Loughborough University, Loughborough LE11 3TU, UK
[c] College of Engineering, University of Swansea, Swansea, UK
[d] GE Power, Rugby CV21 2NH, UK

ARTICLE INFO

ABSTRACT

Oxidation-promoted crack growth, one of the major concerns for nickel-based superalloys, is closely linked to the diffusion of oxygen into the crack tip. The phenomenon is still not well understood yet, especially the full interaction between oxygen diffusion and severe near-tip mechanical deformation. This work aimed at the development of a robust numerical strategy to model the full coupling of crystal plasticity and oxygen diffusion in a single crystal nickel-based superalloy. In order to accomplish this, finite element package ABAQUS is used as a platform to develop a series of user-defined subroutines to model the fully coupled process of deformation and diffusion. The formulation allowed easy incorporation of nonlinear material behaviour, various loading conditions and arbitrary model geometries. Using this method, finite element analyses of oxygen diffusion, coupled with crystal plastic deformation, were carried out to simulate oxygen penetration at a crack tip and associated change of near-tip stress field, which has significance in understanding crack growth acceleration in oxidation environment. Based on fully coupled diffusion-deformation analyses, a case study was carried out to predict crack growth rate in oxidation environment and under dwell-fatigue loading conditions, for which a two-parameter failure criterion, in terms of accumulated inelastic strain and oxygen concentration at the crack tip, has been utilized.

1. Introduction

Diffusion of oxygen into the material under stresses can be found in structural materials working at high temperature. The process leads to degradation of the material properties and development of cracks in the components, which impede the expected performance of the structures and limit their targeted service life [1–3]. Therefore, it is vital to study the interaction of oxygen diffusion and mechanical deformation of high-performance material systems working under high temperatures and severe stresses during their service life. Nickel-based superalloys are used as turbine discs and blades in the hot section of gas turbine engines. These structural components are prone to oxidation damage due to high temperature and fatigue loading environments, especially at a crack tip, which leads to the reduced fatigue life as evident from the literature [4–6].

Gaseous diffusion into material subjected to mechanical deformation has been studied for decades, with the work of Sofronis and Mcmeeking [7] regarded as one of the earliest in this domain. They considered the simultaneous effects of elastoplastic deformation and hydrogen trapping (associated with plastic strain) on hydrogen diffusion in the vicinity of a blunting crack tip. They found that the total hydrogen concentration decreased with the increasing distance from the crack tip. In the work of Mulin et al. [8], the influence of external mechanical loading on oxygen diffusion was studied during the oxidation of nickel. It was observed that the mechanical load led to higher level of oxygen concentration in the oxide scale, and constant load (creep) caused the increased depth of oxygen penetration into the substrate. The development of cracks at the surface nickel oxides under mechanical load was reported by Berger et al. [9], who also mentioned that oxygen diffusivity increased by two orders of magnitude due to the development of multiple cracks in the oxide layer. Additionally, an enhanced level of oxidation in pure nickel was observed during thermogravimetric analysis when subjected to external load. Several studies were performed along these lines to explain the enhanced crack growth rate in nickel alloys under a combined effect of stress and oxidation as compared to that in vacuum [10–12]. It was found that the oxidation was strongly enhanced by mechanical loading [10], and the tensile stress at the crack tip drove more oxygen into the material which

attacked the grain boundaries and introduced the accelerated inter-granular cracking. Recently, simulations were also carried out to predict the stress-assisted oxidation and the associated diffusion of oxygen along the grain boundaries. For instance, Zhao [13] simulated the penetration of oxygen along grain boundaries and demonstrated that the penetration of oxygen into the material is facilitated by the presence of mechanical stress. Additionally, he reported that oxygen tends to accumulate around the crack tip due to the presence of stress singularity. Karabela et al. [14] used the stress-assisted oxygen diffusion along grain boundaries to model the oxidation-assisted fatigue crack growth. Based on the consideration of both the accumulated inelastic strain and the oxygen concentration near the crack tip, a failure curve was proposed and utilized for crack growth prediction under fatigue-oxidation conditions. However, all these studies considered merely the effects of stress on diffusion, called sequential coupling or one-way coupling [7–14], while neglected the effects of oxygen diffusion on deformation.

The full-coupling between mass-diffusion and deformation can be dated back to the work by Yang [15], in which the previous one-way coupling work by Prussin [16] was extended by incorporating the inclusion energy into the chemical potential of the migrating particles. Thus, the localised stress was affected by the rate of migration of external particles into the material. The distribution of external particles affected deformation through geometric mismatch. Another study was proposed based on an electrostatic theory, in which alien particles in a matrix material induced stress through two mechanisms, namely, strain induced by the geometrical incompatibility and Maxwell stress due to the charge carried by the particle [17]. These studies were based on elastic behaviour of the material. In order to overcome this issue, studies were recently carried out to incorporate the plastic behaviour of the material [18,19]. Zhang et al. [18] studied the concurrent large deformation and mass transport for gels using finite element method. They used modified version of the thermodynamics theory, originally developed by Gibbs [19], by considering the non-equilibrium thermodynamics between the solids and liquids rather than equilibrated approach developed by Gibbs. Using this approach, they studied the swelling behaviour of partially constrained gels. More recently, An et al. [20] developed a platform at continuum level to study the full coupling of large deformation and mass diffusion in electrodes for lithium ion batteries. This numerical platform was capable to model the coupled deformation and diffusion behaviour in electrodes which underwent very specific type of mass diffusion based on electrostatic charge and mechanical loading. However, all the studies discussed above did not claim any capability to simulate the damage and fracture of the material under combined effect of deformation and mass diffusion. Thus, to authors' knowledge, a numerical platform that is able to rigorously couple the important factors, namely fatigue deformation and mass diffusion at the crack tip, in structural applications of nickel based alloys is not available to the research community, though there are many related publications on coupled deformation and mass diffusion analyses [15,18,20]. More importantly, the numerical platform must have the capability of extending the study to fracture and damage of alloys under various loading conditions, which makes this task even more challenging.

The objective of the present paper is to simulate the fully coupled stress-diffusion process for Ni based superalloy at a crack tip, namely the single crystal superalloy, MD2. MD2 is a 3rd generation single crystal alloy developed by GE Power for industrial gas turbine applications and without the addition of Rhenium. This paper is organised as follows. In Section 2, a theoretical framework and numerical implementation of mechanical deformation is addressed using crystal plasticity, which is interfaced with ABAQUS via a user-defined material subroutine (UMAT). Section 3 details the mass diffusion analysis, which is based on a rigorous analogy between the mass diffusion and heat transfer in the presence of mechanical stresses. Section 4 deals with the sequential coupling between mechanical and diffusion analysis to account for the effects of deformation on the diffusion during fatigue

loading. This section also studies the fully coupled deformation-diffusion process and results are compared with those obtained from sequentially coupled analysis. Results and discussions are given in Section 5, including a case study on prediction of crack growth rates in fatigue-oxidation environment.

2. Material model

2.1. Constitutive relations

For the crystal plasticity framework used in this work, the total deformation gradient F is decomposed into two multiplicative components, i.e., the elastic part (F^e) and the plastic part (F^p), respectively [21]. The elastic part is associated with the elastic deformation of the material. While the plastic part, as well as the plastic velocity gradient L^p, is related to the shear deformation via [22]:

$$L^p = F^p F^{p^{-1}} = \sum_{\alpha=1}^{n} \dot{\gamma}^\alpha (\mathbf{s}^\alpha \otimes \mathbf{m}^\alpha) \tag{1}$$

where $\dot{\gamma}$ is shear strain rate of slip system α, and $\mathbf{s}^\alpha$ and $\mathbf{m}^\alpha$ are unit vectors along and normal to the slip direction, respectively.

The flow rule, i.e., the inelastic shear strain rate $\dot{\gamma}^\alpha$, for each slip system can be expressed by [22]:

$$\dot{\gamma}^\alpha = \dot{\gamma}_0 \exp\left[\frac{-F_0}{\kappa\theta} \left\langle 1 - \left\langle \frac{|\tau^\alpha - B^\alpha| - S^\alpha \mu/\mu_0}{\hat{\tau}_0 \mu/\mu_0} \right\rangle^p \right\rangle^q \right] \mathrm{sgn}(\tau^\alpha - B^\alpha) \tag{2}$$

where κ is the Boltzmann constant, θ is the temperature, and S^α and B^α are the two scalar state variables representing slip resistance and back stress, respectively. The shear modulus μ and μ_0 refers to that at temperature θ and 0 (in Kelvin), respectively. Other model parameters include F_0, $\hat{\tau}_0$, p, q and $\dot{\gamma}_0$ which need to be determined from experimental data.

The slip system resistance (S^α) evolves according to following relation [22–24]:

$$\dot{S}^\alpha = [h_s - d_D(S^\alpha - S_0^\alpha)]|\dot{\gamma}^\alpha| \tag{3}$$

where S_0^α refers to the initial slip resistance of a slip system, h_s is a material constant associated with static recovery and d_D is another material constant but linked to dynamic recovery.

The back stress evolves according to a standard hardening-dynamic recovery format [22–24]:

$$\dot{B}^\alpha = h_B \dot{\gamma}^\alpha - r_D B^\alpha |\dot{\gamma}^\alpha| \tag{4}$$

where h_B is the hardening constant and r_D is a dynamic recovery constant.

2.2. Model parameters and UMAT

The above constitutive relationship was implemented into the finite element (FE) package ABAQUS via a user-defined material subroutine (UMAT), where the fully implicit (Euler backward) integration algorithm was adopted to interface with a finite element package (ABAQUS) for modelling of cyclic deformation in this work.

A single 3D element, C3D8 in ABAQUS which is eight-node quadrilateral isoparametric element, was used to model the stress-strain response of MD2. The element was subjected to strain-controlled loading where both octahedral and cubic slip systems were considered. Values of the model parameters were calibrated against the uniaxial experimental data of MD2 alloy at 850 °C, measured under strain-controlled loading conditions. These parameters were obtained by minimising the difference between the experimental data and corresponding simulation results.

3. Modelling of oxygen diffusion

3.1. Governing equations

The diffusion of gases into the metals can be given by the extended Fick's law which considers that the flux is proportional to the gradient of chemical potential at current state [20,25]:

$$J_{\text{flux}} = -\frac{DC}{RT}\nabla\mu \tag{5}$$

where J_{flux} is the oxygen flux, D is the diffusivity, C is concentration, R is the universal gas constant, μ is the chemical potential, and ∇ represents the spatial gradient. Here diffusion is assumed to be driven by the gradient of chemical potential. In general, for a system under external stress and in conditions where (5) is valid, chemical potential at constant pressure and temperature [7] is given as:

$$\mu = \mu_\sigma + RT\ln\phi + p\overline{V} \tag{6}$$

where μ_σ is the stress dependent part of chemical potential, p is the hydrostatic stress (pressure), $\overline{V}$ is the partial molar volume of solute and ϕ is the solute concentration (C) normalised by the its solubility (s). It is assumed here that the diffusion causes only dilation to the lattice.

Substituting (6) into (5) and considering the normalised concentration, we find

$$J_{\text{flux}} = -sD\nabla\phi - DM\nabla p \tag{7}$$

where the pressure factor M is defined as

$$M = \frac{\phi\overline{V}}{RT} \tag{8}$$

The constitutive law (Eq. (7)) has been used to account for the influence of mechanical stress on mass transport [25–27]. The gradient of hydrostatic pressure is regarded as the driving force for stress-assisted diffusion process. In the absence of pressure stress effects, i.e., the pressure factor $M = 0$, the formulation is reduced to natural diffusion. The deformation-assisted diffusion is thus defined by specifying the hydrostatic stress in chemical potential (Eq. (6)) and the pressure factor in flux (Eq. (7)). In this paper, the pressure factor was treated as a single parameter due to the difficulty of obtaining physically-meaningful value of partial molar volume of oxygen in the formed oxides.

3.2. Mass diffusion and heat transfer analogy

In order to implement the theoretical model mentioned in Section 3.1 in ABAQUS, thermal diffusion is utilized to model the mass diffusion through the analogy between the two transport phenomena, dated back to Prussin in 1960s [16]. The terminologies and description of governing equations used for the mass diffusion and heat transfer are discussed here to clarify the analogy of the two transport phenomena [28].

The conduction-based heat transfer can be described by Fourier's law,

$$q = -k\nabla T \tag{9}$$

where T, k and q are the temperature, thermal conductivity and heat flux, respectively. Assuming no internal heat generation, the energy balance yields the governing equation of heat transfer as

$$\rho C_p \frac{\partial T}{\partial t} + \frac{\partial f}{\partial x} = 0 \tag{10}$$

where ρ is the density, C_p is the specific heat and f is the true heat flux.

Considering no mass is generated, the mass conservation yields the governing equation of mass diffusion (Fick's second Law) as

$$\frac{\partial C}{\partial t} + \frac{\partial J_{\text{flux}}}{\partial x} = 0 \tag{11}$$

By comparing Eq. (10) for heat transfer and Eq. (11) for mass

Table 1
Heat-transfer and mass diffusion analogy scheme.

Field Variable	Heat Transfer	Mass Diffusion
Temperature	T	C
Density	ρ	1
Conductivity	k	D
Specific heat	C_P	1

diffusion, it is clear that mass diffusion is analogous to heat transfer by the equivalence given in Table 1.

This specifically designed heat transfer behaviour is implemented in ABAQUS via its user-defined heat transfer subroutine UMATHT. This subroutine receives temperature T (or equivalent C in this analogy) and its time gradient $\partial T/\partial t$ (i.e., $\partial C/\partial t$) from ABAQUS and also defines the heat flux f (i.e., J_{flux}).

4. Numerical implementation

In order to implement the theoretical model presented in Sections 2 and 3, a robust numerical method is required, and can be used not only to gain insight of the mechanisms involved in stress-oxidation damage but also to predict the life of the structural components under combined effects of these loading conditions. Two types of analyses, sequentially coupled and fully coupled mechanical-diffusion analyses, are described in this section.

4.1. Sequentially coupled analysis

For sequential coupling analysis, both stress and diffusion were computed in single analysis. During the stress analysis, a crystal plasticity based subroutine (UMAT) was used and stress-assisted mass diffusion was calculated using a subroutine called UMATHT. A flow chart is shown in Fig. 1, which illustrates the procedure to carry out sequentially coupled stress-assisted diffusion using subroutine. As discussed in Section 3, the gradient of hydrostatic stress is required to calculate the stress-assisted oxygen diffusion. This gradient was calculated by considering the average nodal value of hydrostatic stress for each node by using a subroutine URDFIL in ABAQUS. This subroutine has the capability to obtain the specific results from the previous increment during the analysis. These results are generally written in a file specified by ABAQUS (file extension is ∗.fil). Therefore, the URDFIL subroutine is called at the end of each increment for accessing the result file. In details, the average nodal values of hydrostatic stress are read from the result file, and their gradients are calculated using the Jacobian transformation matrix that connects the global coordinates (x,y) to the local coordinates (ξ,η). The overall procedure to compute pressure gradient is given in a subset of Fig. 1, with mathematical form summarised in Appendix A.

In summary, the pressure calculated from UMAT is used in URDFIL to calculate the pressure gradient which is ultimately used as input for UMATHT. The stress-assisted oxygen diffusion is computed using the UMATHT. This process continued until the targeted simulation time was achieved. Solution-dependent variables were used to store and share 3 normal stress components and oxygen concentration across all three subroutines (UMAT, UMATHT and URDFIL). Also, common blocks were used for transferring the data among the subroutines.

4.2. Fully coupled analysis

In a general stress-oxidation problem, a fully coupled analysis is required to understand the dependence of stress state on oxygen diffusion and vice versa. In contrast to sequentially coupled analysis, the effects of mass diffusion on the deformation are considered along with the effect of mechanical deformation on mass diffusion for fully coupled
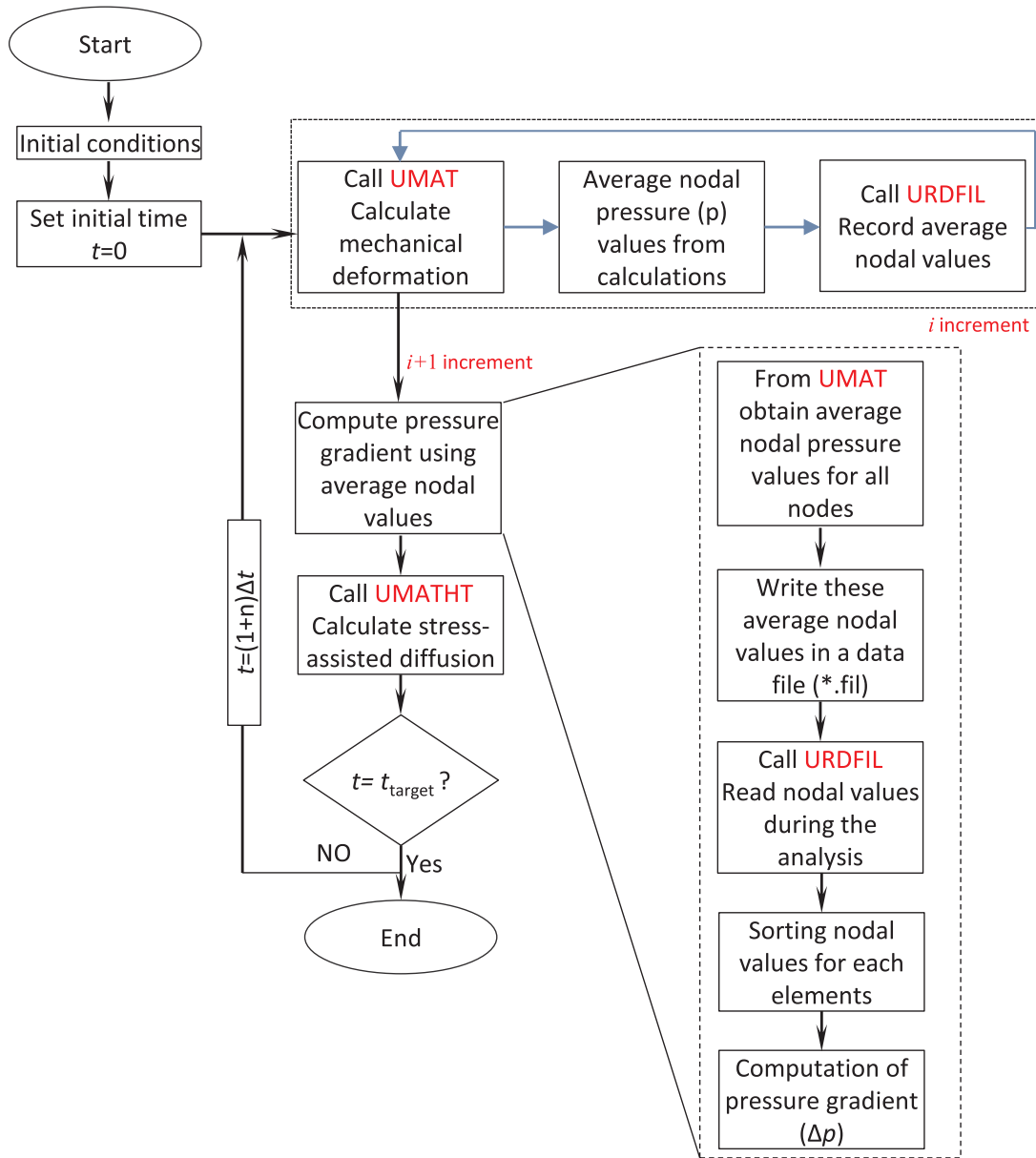
Fig. 1. Flow chart of numerical scheme for sequential coupling (based on subroutine UMAT and UMATHT).

analysis. To implement the effect of mass diffusion on stress-state, the thermal expansion in heat transfer that is analogous to the compositional expansion in mass transfer is considered here via ABAQUS. Assuming isotropic compositional expansion, the compositional expansion strain caused by dilation or swelling is given as

$$\varepsilon_{\text{compositional}} = \beta \Delta C \qquad (12)$$

where β is the expansion coefficient and ΔC is the change in oxygen concentration. This compositional strain is embedded in ABAQUS using its user-defined thermal expansion subroutine UEXPAN.

Similar to sequential coupling analysis procedure, fully-coupled analysis also employed UMAT, UMATHT and URDFIL to define the constitutive behaviour, mass diffusion (based on analogy with heat transfer) and hydrostatic pressure gradient, respectively. In addition to these, another subroutine UEXPAN was used to capture the effect of oxygen diffusion on stress caused by compositional expansion or dilatation. A flow chart showing the procedure to carry out fully coupled stress-assisted diffusion using subroutine is shown in Fig. 2.

In all simulations, the number of iteration at a given time and the criterion for numerical convergence check are automatically controlled by ABAQUS. For coupled deformation-diffusion analyses, ABAQUS has a tolerance of 5×10^{-3} for guaranteeing the system's equilibrium (force, momentum and flux). Overall, if the tolerance is not satisfied at a given time within the allowed number of iteration, the time increment will be cut back by ABAQUS automatically (by a factor of 0.25) and the iteration process will be repeated until the tolerance is satisfied. In our analyses, the maximum number of equilibrium iterations was set to be 16 and the maximum time cut-backs allowed in an increment was set to be 20, which are sufficient to achieve the numeral convergence. It should be noted that the major effort in this paper is to programme the URDFIL subroutine to compute the pressure gradient based on average nodal values. This pressure gradient is required for UMATHT to calculate stress-assisted diffusion.

4.3. Finite element model and mesh

In order to perform sequentially and fully coupled analysis, a three-point bending specimen with dimensions shown in Fig. 3 was considered. The specimen has a [0 0 1] orientation in the x direction and
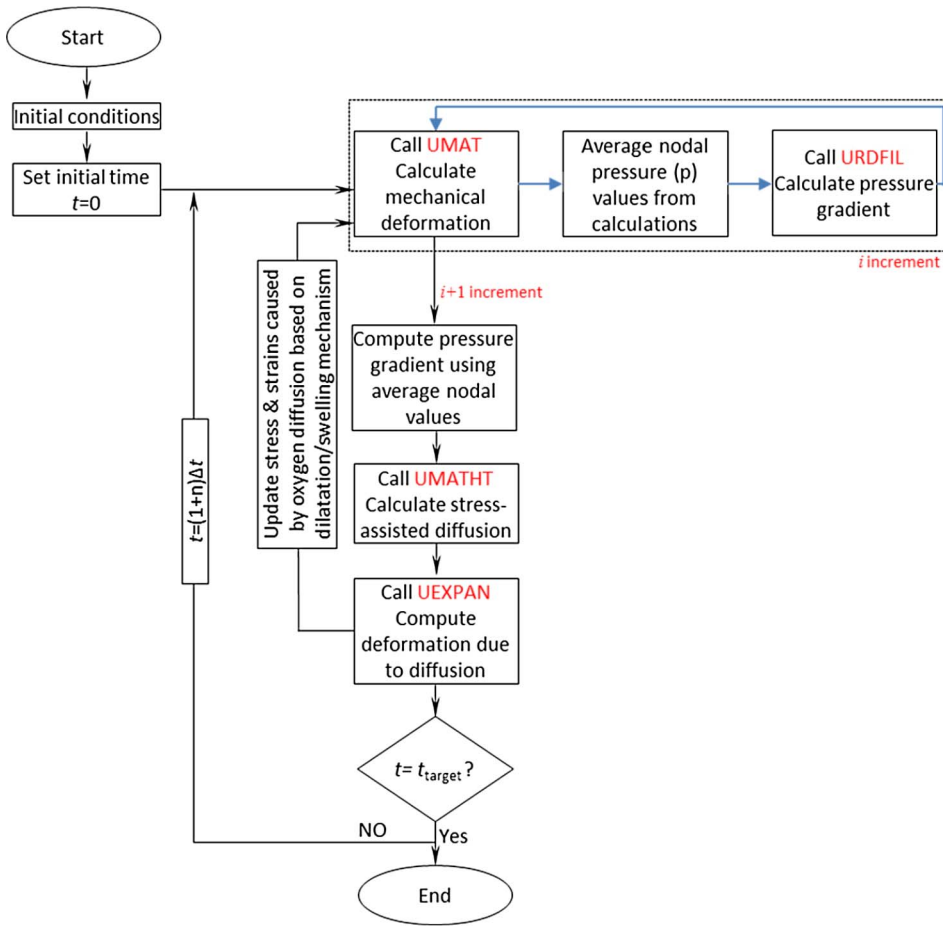
F. Farukh et al.

Fig. 2. Flow chart of numerical scheme for fully coupled analysis (based on subroutines UMAT, UMATHT, UEXPAN and URDFIL).
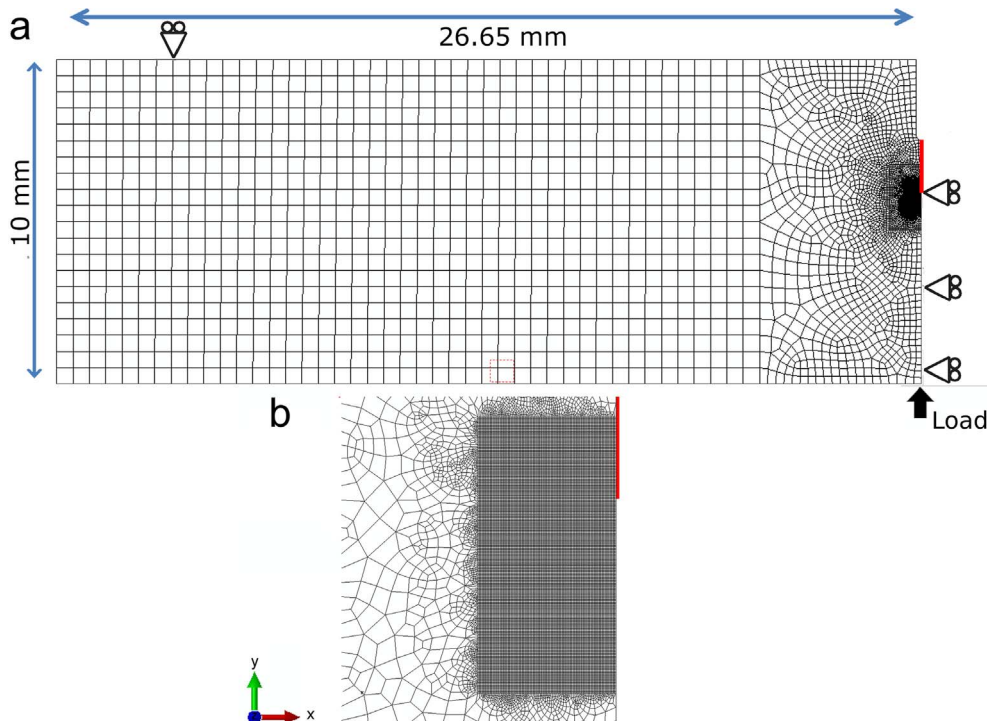

Fig. 3. Finite element model for deformation-diffusion analysis: (a) mesh for single edge notched beam sample; (b) refined mesh near crack tip (red line shows crack).

Table 2
Parameters used in diffusion analysis.

Parameter	Value
Diffusivity (D)	1.5×10^{-10} (mm^2/s)
Pressure factor (M)	0.1 (MPa^{-1})

[0 1 0] orientation in the y direction (Fig. 3). A monotonic load of 3.2 kN with loading time of 3600 s was applied to the middle node on the bottom side of the specimen (Fig. 3) which is also constrained in the x-direction to avoid the rigid body motion. While the two supports on the top side of the specimen are constrained in the y-direction to avoid rigid body rotation. In order to reduce the computational cost, only one half of the model was considered for the simulations. This maximum load of 3.2 kN corresponds to a stress intensity factor range of $\Delta K = 25.37$ MP$\sqrt{m}$. The initial crack introduced to the model was chosen to be $a = 4$ mm, i.e., $a/W = 0.4$, which includes the notch with a depth of 2.5 mm and a pre-crack of 1.5 mm. The parameters required for the diffusion analysis, i.e. oxygen diffusivity (1.5×10^{-10} mm^2/s) and pressure factor (0.1 MPa^{-1}), are given in Table 2. These values were taken from one of our previous paper [14]. In that paper, the depth of internal oxidation under variable cyclic stress levels was measured from the fatigue-oxidation tests on waisted specimens of a nickel alloy. The measurements had been subsequently used for the determination of the two essential parameters (diffusivity and pressure factor) based on the simulation of oxygen penetration along grain boundaries under the influence of heterogeneous ploycrystal plasticity deformation. Values given in Table 2 are within the range reported in [14]. The thermal expansion coefficient to realize the desired compositional expansion was taken as $\beta = 10^{-3}$ mm^3/g. The concept of thermal expansion is used to account for the compositional expansion caused by oxygen diffusion, which is similar to the work of Aslan [29] who modelled the process of hydrogen diffusion. Unfortunately, physical measurement is not available for this parameter. We simply estimated the value based on the stress level produced at the crack tip by the oxidation process. Here, we aimed at a stress level of tens of MPa, as predicted by Suo et al. [30] for free surface oxidation process.

The finite element mesh in the near tip region is shown in Fig. 3b, which was surrounded by a coarser mesh. For crack growth, it is recommended that the mesh should be fine enough to capture the cyclic (after load reversal or at the minimum load level) inelastic zone so that crack tip can be effectively evaluated [31]. In the present study, the inelastic zone is around 10 μm after load reversal (compared to ~50 μm at the peak load level). In order to capture this properly, a fine mesh zone (around 1 mm) was created near the crack tip (Fig. 3b), and the element size in this fine mesh zone is 5 μm which is small enough to capture the cyclic inelastic zone. This element size is over ten times bigger than the precipitate's size (~0.4 μm) of MD2, allowing us to model the material using the continuum crystal plasticity theory. A total of 17,574 four-node quadrilateral isoparametric elements were used with 17,716 nodes. The type of the elements used for all the coupling analysis in this study has temperature as an additional degree of freedom. Specifically, element C2D4T in ABAQUS is used throughout the coupled simulations in this paper. This element has 4 nodes and 4 integration points. However, any element with coupled displacement and temperature as active degree of freedom can be utilized. Exactly the same mesh was used for all the coupled simulations in this study. In order to simulate the mass diffusion analyses, an initial value of oxygen concentration at the crack surface was chosen as 1 g/mm^3. For all the mechanical deformation analyses, a concentrated load is applied to the middle node on the bottom side of the specimen (Fig. 3) which is also constrained in the x-direction to avoid the rigid body motion.

5. Results and discussion

5.1. Calibration of model parameters

The identification of material parameters began with a step-by-step procedure to obtain an initial set of parameters. The experimental results were used as inputs. Low cycle fatigue tests were carried out using standard cylindrical specimens (diameter of 6.4 mm and gauge length of 36.5 mm) at a temperature of 850 °C to reflect the working environment of nickel superalloys. The specimens were subjected to strain-controlled cyclic loading, with 2 s-2 s-2 s-2 s (2 s dwell at both maximum and minimum load levels) and 200 s-200 s-200 s-200 s (200 s dwell at both maximum and minimum load levels) loading waveforms, along ⟨0 0 1⟩ direction. The maximum level of strain applied on the element was 1%, with a strain ratio of −1. In this work, the crystallographic formulation constitutes on 12 octahedral slip systems. The procedure consists of a series of iterations until an acceptable tolerance is achieved between model simulations and experimental data.

The components of stiffness C_{11}, C_{12} and C_{44} were first evaluated using the elastic response of the material from the FE analysis of the single 3D element under monotonic loading. The values of these stiffness components were found to be $C_{11} = 171.03$ GPa, $C_{12} = 104.38$ GPa and $C_{44} = 103.52$ GPa. The material flow rule coefficients were then calibrated by fitting the stress-strain response of the material under monotonic, stress-relaxation and cyclic tests. The parameters associated with the flow rule include p, q, F_0, $\dot{\gamma}_0$, f_c and β. After an initial estimate of the unknown material parameters, subsequent iterations were performed until a consistent description of the experimental data set was obtained. The material constants associated with the internal slip system variables, namely h_s, d_D, h_B and r_D, were calibrated in a manner similar to that outlined above. Cyclic hardening behaviour is of great importance for materials under cyclic deformation and requires strenuous efforts in parameter calibration. In this study, extensive FE analyses were carried out in order to obtain the good description of cyclic deformation.

The parameter values, calibrated from the test data, are listed in Table 3. Comparisons of the experimental data and the model simulations along ⟨0 0 1⟩ direction are given in Figs. 4 and 5 for the first cycle and the cyclic hardening behaviour of the material. Clearly, the model predictions are in close agreement with the test data. Furthermore, the shape of the hysteresis loop and cyclic softening is also well reproduced by the crystal plasticity model. Thus, the model is capable of providing a good prediction of the material mechanical behaviour over different loading rates.

5.2. Sequential coupling

The contour plot presented in Fig. 6a shows the oxygen concentration obtained from subroutine-based sequentially-coupled analysis (UMAT and UMATHT). In order to verify the results, finite element

Table 3
Values of fitted parameters for crystal-plasticity constitutive model at 850 °C.

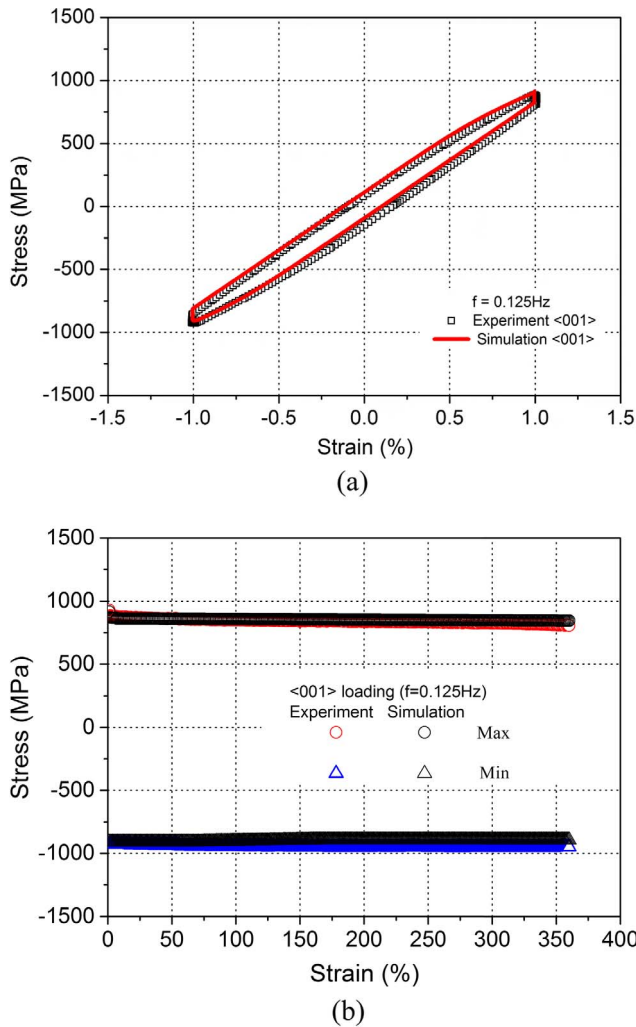| Parameters	Octahedral slip
p	0.5
q	1.8
F_0 (kJ/mol)	236
$\dot{\gamma}_0$ (s^{-1})	525
$\hat{\tau}_0$ (MPa)	4600
f_c	0.2
S_0 (MPa)	400
h_b	200
h_s	160
r_D	190.41
d_D	233.4

(a)

(b)

Fig. 4. Comparison of simulated results and experimental data for (a) the first cycle and (b) cyclic hardening along ⟨0 0 1⟩ (strain rate = 0.5%/s and strain range = 1%).

(a)

(b)

Fig. 5. Comparison of simulated results and experimental data for (a) the first cycle and (b) cyclic hardening along ⟨0 0 1⟩ (strain rate = 0.005%/s and strain range = 1%).

analysis was also carried out by using the method already available in ABAQUS. Basically, the UMAT was used to obtain the hydrostatic pressure first, followed by diffusion analysis. In ABAQUS, the stress-driven oxygen diffusion was also accounted for through Eq. (7) which considers the gradient of hydrostatic pressure. A contour plot of the oxygen concentrations around the crack tip is shown in Fig. 7, which is very similar to that obtained from our procedure (Fig. 6a). Additionally, the maximum values of oxygen concentration obtained from the two methods are in very good agreement. The two methods are essentially the same. In ABAQUS, the pressure gradients are calculated automatically, and then used to model the effect of mechanical deformation on oxygen diffusion. In this paper, a URDFIL subroutine was written to compute the pressure gradients from the stress analysis results. We compared the two methods solely for the purpose of validating the correctness of URDFIL subroutine that was written by ourselves, as confirmed by the good agreement (Fig. 6a and 7). In addition, Fig. 6b–d shows the contour plots of the hydrostatic pressure and its gradient in the vicinity of the crack tip which was required for stress-assisted diffusion analyses. It should be noted that sequential coupling analyses did not account for the effect of diffusion on mechanical deformation.

To understand the effect of hydrostatic pressure in connection with Eq. (7), analysis of natural diffusion of oxygen was carried out. This was realised by neglecting the mechanical deformation analysis stage in sequential coupling analysis and only the diffusion was considered. Oxygen concentration around the crack tip in natural diffusion analysis
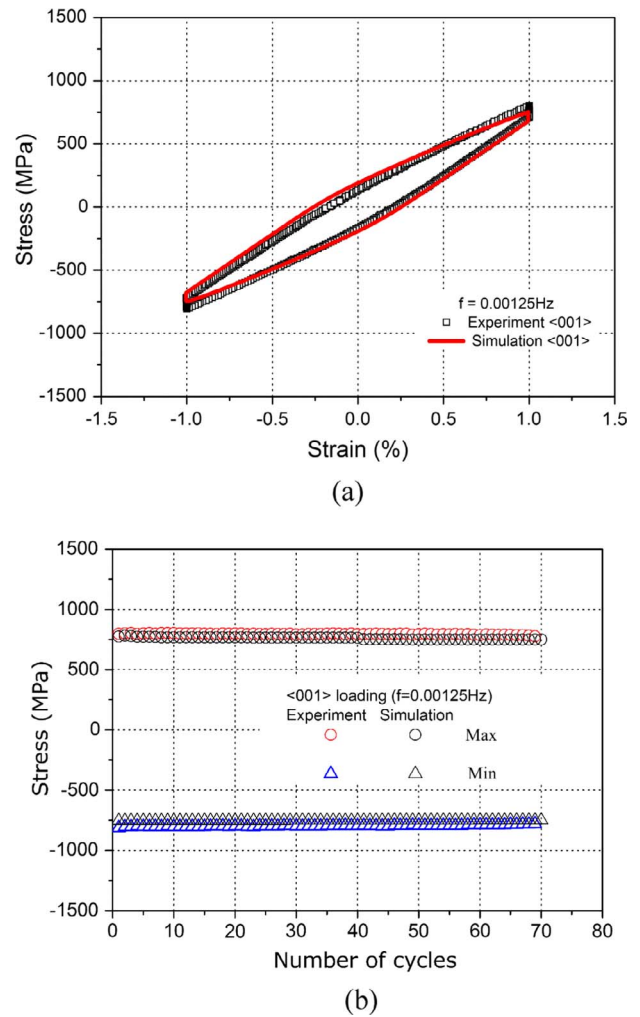
is shown in Fig. 8. By comparing the results shown in Figs. 6a and 8, it was observed that sequential coupled analysis showed higher level of oxygen diffusion as compared to that of natural diffusion, as stress tends to increase the oxygen diffusion in front of crack tip. This clearly demonstrates that the oxygen diffusion is enhanced by the stress (hydrostatic pressure). This phenomenon is linked to the fact that lattice sites are stretched by the stress, causing higher oxygen diffusion at those locations.

5.3. Full coupling

The distribution of oxygen concentration and opening stress around the crack tip is shown in Fig. 9a and b for fully coupled deformation and diffusion analyses. It was observed that the maximum value of stress around the crack tip in fully coupled analysis is lower than that in sequentially coupled analysis. This can be attributed to the fact that the compressive stress caused by swelling due to oxygen diffusion cancels out part of the tensile stress caused by mechanical deformation. Since there was no effect of dilatation on the deformation in sequentially coupled analysis, a higher value of stress was observed in sequentially coupled analysis. Subsequently, the maximum value of oxygen concentration in fully coupled analysis is also less than that of sequentially coupled analysis. Since the oxygen concentration and its distribution in fully coupled analysis are different from those in sequential analysis (see Fig. 6a and 9a), it is clear that the oxygen transport is affected by the hydrostatic pressure. The deformation of the material under
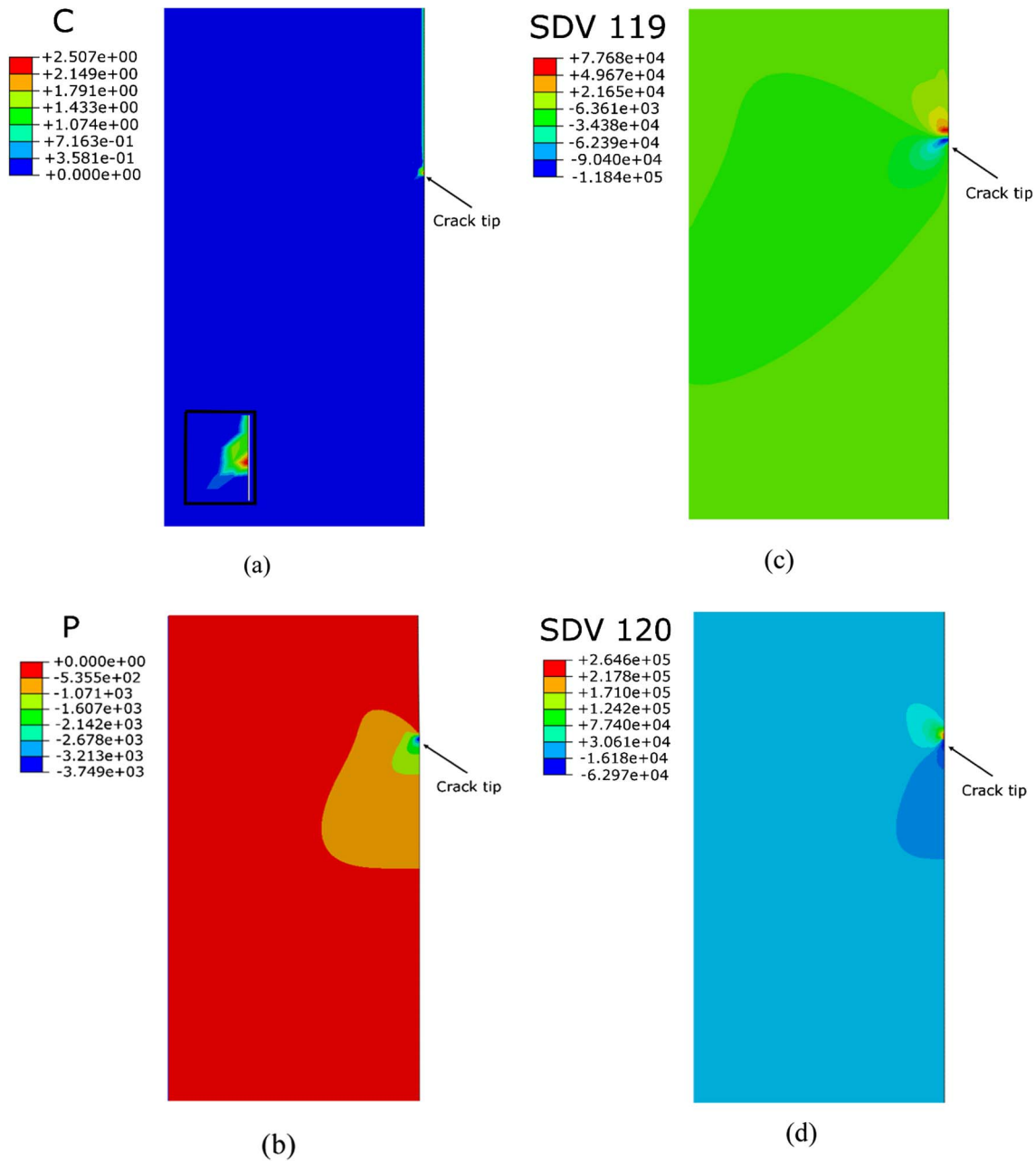
Fig. 6. The contour plots of (a) oxygen concentration (g/mm³), (b) hydrostatic pressure (MPa), (c) pressure gradient (MPa/mm) parallel to crack and (d) pressure gradient (MPa/mm) perpendicular to crack for sequential coupling analysis (K = 25.37 MPa√m and loading time t = 3600 s).

mechanical load causes tensile hydrostatic stress (i.e., negative pressure) and facilitates the transportation of oxygen into the material. This is analogous to a pipette in which negative pressure means 'pump in' and positive pressure means 'squeeze out'. The reason for the reduced oxygen concentration in fully coupled analysis is the lower value of hydrostatic stress at the crack tip in fully coupled analysis (see Fig. 9c) as compared to that in sequentially coupled analysis (Fig. 6b). It can be attributed to the fact that the dilatation or swelling of the material caused by the oxygen diffusion produces compressive hydrostatic stress (positive pressure) and restrain the penetration of oxygen into the material. This compressive hydrostatic stress (or positive hydrostatic pressure) developed at the crack tip as a result of oxygen penetration is associated with the constrained volumetric expansion of the local material imposed by the surrounding bulk alloy. Thus, overall hydrostatic stress at the crack tip is reduced resulting in less oxygen penetration.

Physically it can be understood by assuming that the mechanical

deformation tends to open the crack (negative hydrostatic pressure) and more oxygen diffuses into the material. However, the compressive stress state caused by dilatation of the material, as a result of oxygen diffusion, reduces the level of tensile stress at the crack tip (stress intensity factor ΔK). Hence, less oxygen penetrates into the material. As a result, the maximum value of oxygen diffusion obtained from the fully coupled analysis is less than that of the sequentially-coupled analysis (see Fig. 6a and 9a). In order to understand this concept in more detail, consider the case of natural diffusion where no load was applied on the specimen (no mechanical deformation). The boundary conditions for the natural diffusion are similar to those of fully coupled analysis but without any external mechanical load. Oxygen will penetrate into the alloy under natural diffusion process and result in volume expansion on oxide formation. The volumetric strains are developed within the mechanically constrained environment of the surrounding alloy and result in compressive stress, normal to the crack plane, in the vicinity of the
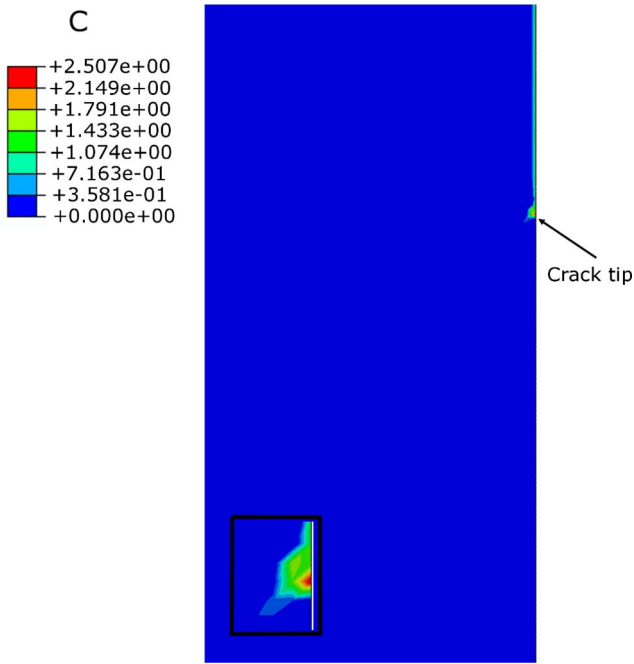
Fig. 7. Contour plot of oxygen concentration (g/mm^3) around the crack tip for sequential coupling using ABAQUS' own procedure (K = 25.37 MPa√m and loading time t = 3600 s).
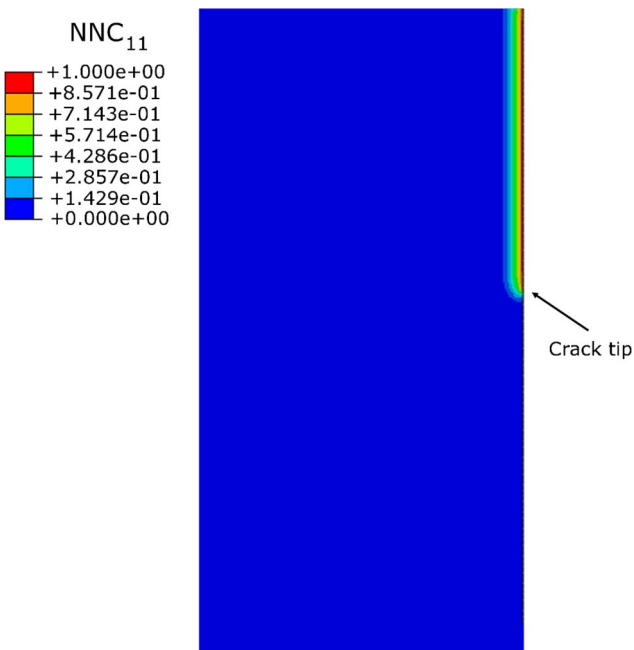

Fig. 8. Contour plot of oxygen concentration (g/mm^3) around the crack tip for natural diffusion (t = 3600 s).

crack tip as shown in Fig. 10a. It is worth noting that the normal stress becomes less compressive with increasing distance from the crack-tip as shown in Fig. 10b. These results are in line with those reported in literature [32].

5.4. Interaction of fatigue and oxygen diffusion

It is important to study the interaction between fatigue loading and oxidation in assessing structural performance of nickel-based super-alloys at high temperature, especially the dwell periods and unloading times, which are not well understood yet.
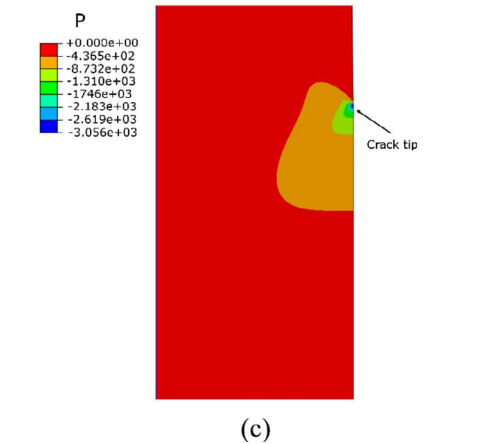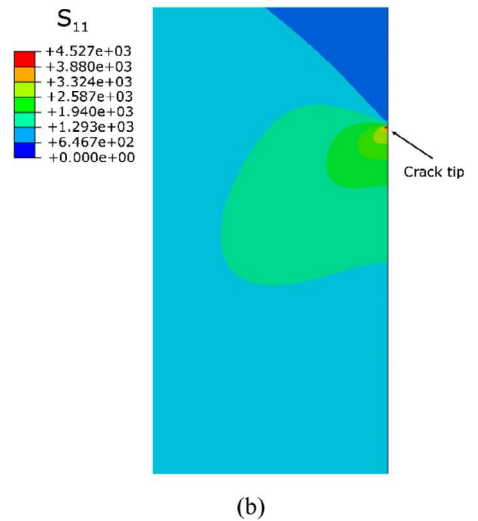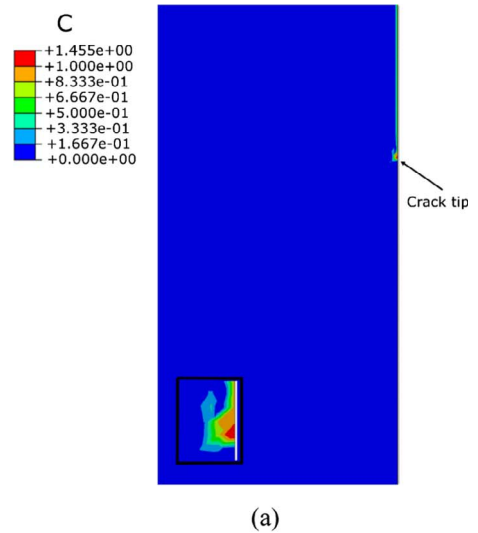

Fig. 9. Contour plots of (a) oxygen concentration (g/mm^3), (b) opening stress (MPa) and (c) hydrostatic pressure (MPa) around the crack tip for fully coupled analysis (K = 25.37 MPa√m and loading time t = 3600 s).

5.4.1. Effect of dwell period

To study the effects of dwell period on oxygen penetration, FE analyses were carried out under fatigue loading conditions using the fully-coupled crystal plasticity-oxygen diffusion model. The stress intensity factor range ΔK = 25.37 MPa√m and load ratio R = 0 were considered for the analysis. Four different dwell loading situations 1 s,
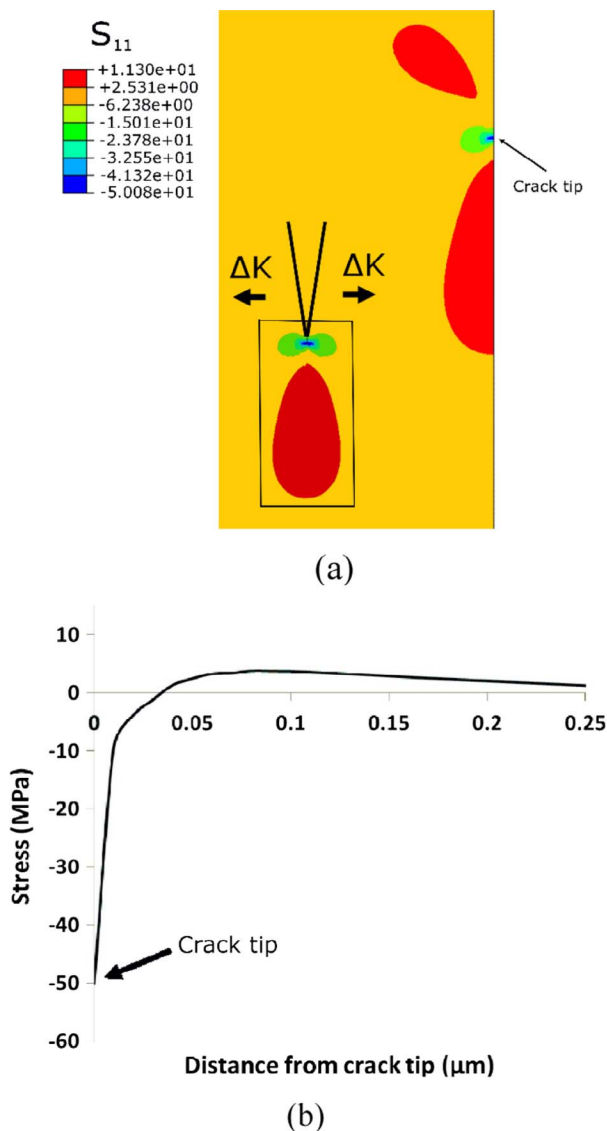
F. Farukh et al.

Fig. 10. Stress caused by diffusion of oxygen into the crack tip: (a) Contour plot of normal stress (MPa) near crack tip and (b) variation of the normal stress ahead of the stationary crack tip.

Fig. 11. Effect of dwell time on (a) crack opening stress and (b) oxygen concentration ahead of a stationary crack tip (loading time = 1 s, ΔK = 25.37 MPa√m, load ratio R = 0, dwell is superimposed on peak load).

900 s, 1800 s and 3600 s were considered, where the dwell was superimposed at the peak load of a simple triangular loading waveform (0.5 Hz).

The maximum value of oxygen concentration at the crack tip and its maximum penetration depth into the material is shown in Fig. 11 for different dwell times. The maximum value of oxygen concentration increases with dwell times, a result of prolonged exposure to oxidation. Additionally, the depth of penetration of oxygen into the material increases with the dwell time. This observation is based on the fact that the crack remains fully open and experiences the highest level of stress during the peak-load hold duration and more oxygen penetrates into the material. Conversely to the oxygen diffusion, the crack opening stress (σ_{11}) is inversely proportional to the dwell time. This phenomenon can be attributed to the compressive stress caused by oxide formation at the crack tip within the mechanically constrained surrounding material as mentioned in Section 5.3. As a result of this compressive stress at the crack tip due to oxidation, the crack opening tensile stress was reduced at longer dwell time. Thus, a lower level of crack opening stress was observed at the end of longest dwell time (i.e. 3600 s) whereas a higher level of stress was observed at 1 s dwell time.
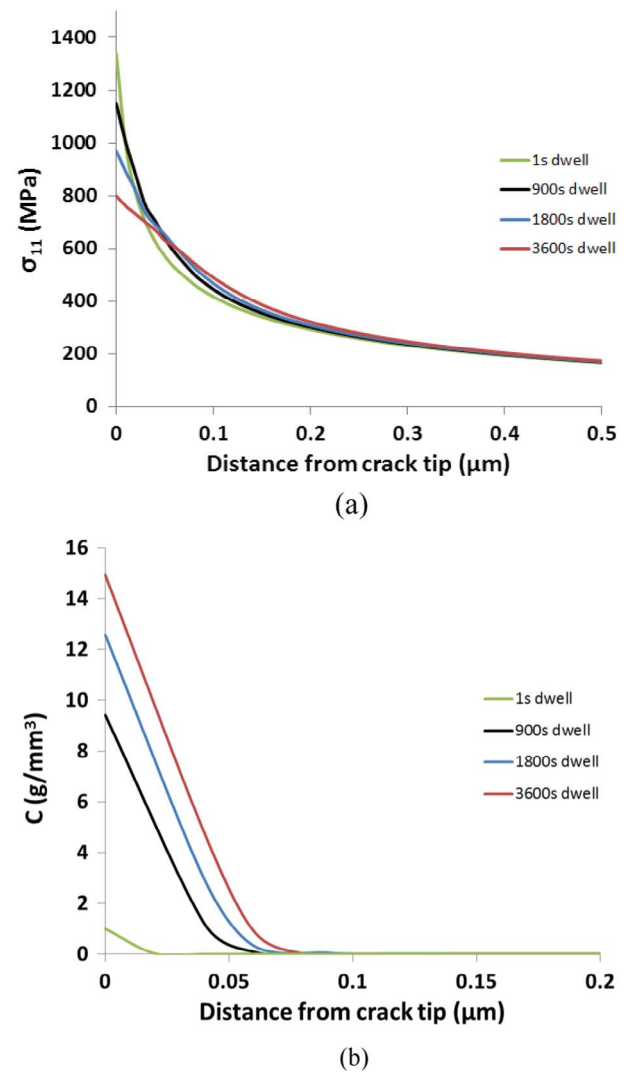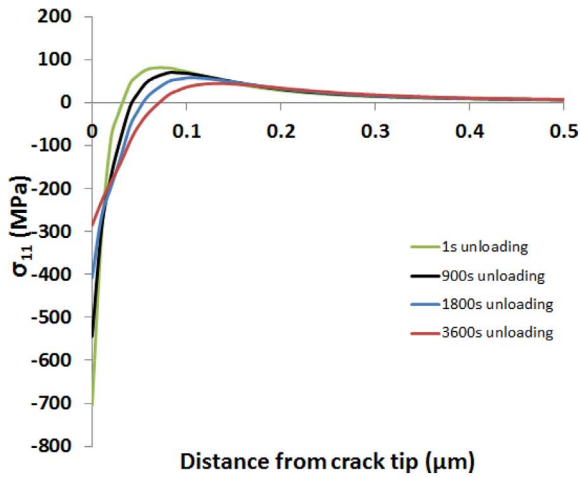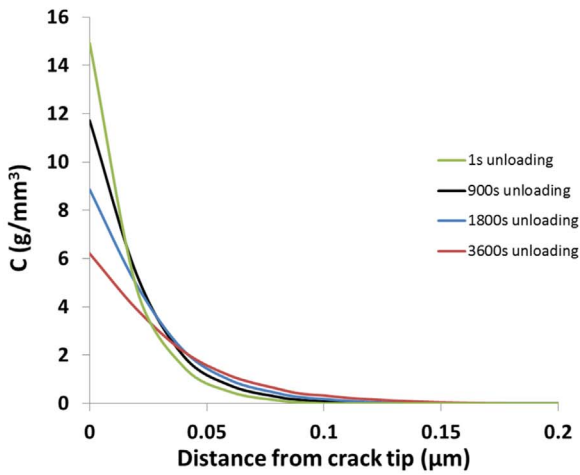
5.4.2. Effect of unloading times

To study the effects of unloading times on oxygen penetration, a loading cycle consisting of 1 s loading time, 1-h dwell period and varied unloading times (1 s, 900 s, 1800 s and 3600 s) was considered in the fully coupled finite element simulations. A stress intensity factor range of 25.37 MPa√m was chosen in this study. The reason for choosing a long dwell (1 h) was to allow more oxygen penetration into the crack tip, which made the effects of unloading time on oxygen diffusion to be observed more obviously.

The maximum values of oxygen concentration at the crack tip and penetration depth into the material are shown in Fig. 12b for different unloading times. The depth of penetration of oxygen into the material increases with the unloading times. However, the maximum value of oxygen concentration decreases with the unloading times (Fig. 12b). Oxygen penetrated into the material during the loading and dwell time when crack is opening. However, during the unloading, the crack tends to close and almost no more oxygen penetrated into the material during that time. Instead, the oxygen already penetrated into the material during loading and dwell period, diffused further into the material and thus the depth of oxygen penetration increased as shown in Fig. 12b. Since only limited oxygen penetrated into the material during unloading, the maximum value of oxygen concentration decreased with increasing unloading time as shown in Fig. 12b. Therefore, minimum

F. Farukh et al.

(a)

(b)

Fig. 12. Effect of unloading time on (a) crack opening stress and (b) oxygen concentration ahead of a stationary crack tip (ΔK = 25.37 MPa√m, load ratio R = 0, loading time = 1 s, unloading follows 3600 s dwell period).

level of oxygen concentration at the crack tip was achieved for 3600 s whereas highest level concentration was achieved for 1 s unloading time. On the other hand, the stress normal to the crack plane became compressive near the crack tip due to oxygen flux (Fig. 12a). The level of compressive stress intended to decrease with the increasing unloading time due to the reduction of oxygen concentration near the crack tip (Fig. 12a).

5.5. Prediction of crack growth rate under dwell fatigue in oxidation environment

An appropriate criterion accounting for both mechanical deformation and oxidation damage is essential in order to predict the crack growth rates under the combined effects of fatigue and oxidation conditions. This requires necessary parameters to represent mechanical deformation and oxidation effect, respectively. In nickel based alloys under fatigue loading conditions, the accumulated inelastic strain has been successfully used as a parameter to predict the crack growth rate in vacuum (without oxidation) and was also adopted in this work. In order to consider the contribution of oxidation to crack growth, oxygen concentration near the crack tip was used as the second parameter in this study.
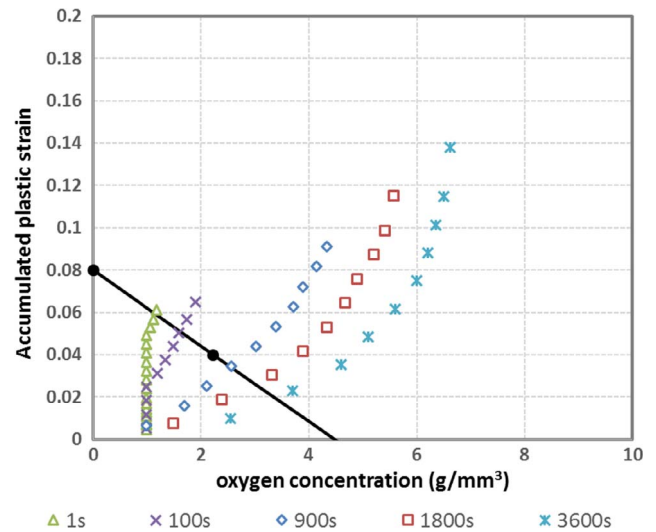

Fig. 13. Accumulated plastic strain vs oxygen concentration at the crack tip for different dwell times with ΔK = 25.37 MPa√m; Failure line in terms of accumulated inelastic strain and oxygen concentration near crack tip is also shown as black line in the figure.

Specifically, FE analyses were carried out for the 3-point bending crack specimen under dwell fatigue. The loading waveform considered was 1-X-1, which means that the sample was loaded to maximum load level in 1 s, held at the maximum load for X seconds (X = 1, 100, 900, 1800 and 3600 s) and unloaded to the minimum load in 1 s. The load ratio was kept as 0.1 and a stress intensity factor range of 25.37 MPa√m was considered. The simulation was run for several number of cycles. The values of both accumulated plastic strain and oxygen concentration, averaged over the element just ahead of the crack tip, were extracted at the end of dwell period in each cycle and plotted against each other. Fig. 13 shows the plot of oxygen concentration vs accumulated plastic strain for ΔK = 25.37 MPa√m. It can be observed from Fig. 13 that the value of accumulated plastic strain continuously increases with number of cycles, however the rate of increase in oxygen concentration ahead of the crack tip gets slower at higher number of cycles. The possible reason for this phenomenon lies in the fact that the oxygen concentration tends to get saturated at crack tip after a certain period of time.

Then the next step is to develop a failure criterion for the prediction of crack growth rate, for which experimental crack growth data in literature was used due to the non-availability of crack growth data for MD2. Specifically, the crack growth rate was chosen to be 5.0×10^{-7} in vacuum under simple fatigue (frequency of quarter Hz) and 1.0×10^{-6} in air under 300 s dwell fatigue (waveform 1 s-300 s-1 s). The number of cycles for crack to grow was then calculated by dividing the near-tip element size (5 μm) with the measured crack growth rate. FE simulations were then run for the calculated number of cycles, i.e., just before the crack grows into the next element, for both cases. The accumulated plastic strain and oxygen concentration were then extracted from these simulations and plotted in the graph as two separate data points (solid circles). A straight line was then drawn to join the two data points which intercepted both x and y axis as shown in Fig. 13. This line was then used as a failure line to predict the crack growth rate under fatigue-oxidation conditions.

Using the failure line constructed above, crack growth rates can be predicted from the finite element analyses for given loading conditions. For ΔK value considered here (i.e., 25.37 MPa√m), the accumulated inelastic strain and the oxygen concentration averaged over the element ahead of the crack tip (i.e., 5 μm) were tracked against the number of fatigue cycles. When the combination of the accumulated inelastic strain and the oxygen concentration reached the failure line, the crack was assumed to grow by one element. The average crack growth rate was then calculated by dividing the element size with the number of
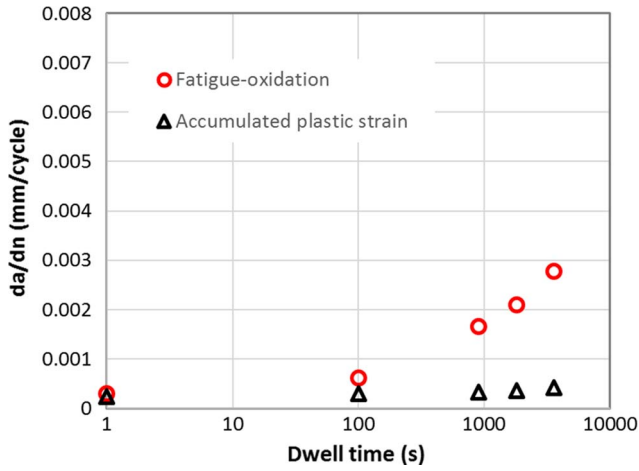
Fig. 14. Predicted fatigue crack growth rate in oxidation environment for different dwell times with ΔK = 25.37 MPa√m; Predicted crack growth rates in vacuum are also included for comparison.

cycles required to reach the failure line. The predicted effects of dwell time on crack growth rates is shown in Fig. 14 in a comparison with the predictions based on mechanical deformation only (i.e., accumulated inelastic strain reaches the critical value). It is noted that based on the failure line, considerable improvements can be achieved in prediction of crack growth rate under fatigue-oxidation conditions.

It should be noted that some parameters (particularly the oxygen diffusivity and pressure factor) are not available yet and were chosen according to some published papers. Thus, this work mainly shows the capability of the proposed numerical approach to model the full coupling of deformation and oxygen diffusion at a crack tip in high temperature alloys. Additionally, it exhibits a potential in predicting the oxidation-accelerated crack growth rate for Ni based alloys under various loading conditions. However, the method has a generic feature and can be used to model the general phenomenon of deformation-diffusion coupling as long as the appropriate constitutive behaviour is identified for the material. Also, mesh size dependency still remains an unresolved issue for simulating crack tip deformation and crack growth. Common practice in fracture mechanics is to choose a length scale to eliminate the element-size dependency. In our case, the length scale can be regarded as the element size near the crack tip, i.e., 5 μm. And the failure curve and crack growth prediction presented in this paper are all associated with this length scale. This length scale should be independent of the change of element size near the crack tip. Specifically, even the element size changes, the failure-curve construction and crack-growth prediction should still be based on this length scale. Then the results will become insensitive to the change of element size near the crack tip.

6. Concluding remarks

In the present work, a finite-element based approach has been developed to model the fully-coupled deformation-diffusion process at a crack-tip in Ni-based superalloys. In order to make this numerical method more robust, it was developed within the framework of commercially available software ABAQUS. In this approach, the coupling was realised by an analogy between heat transfer and mass diffusion in ABAQUS. A real time direct coupling scheme between deformation and oxygen diffusion was formulated using several user-defined subroutines in ABAQUS, namely user-defined material (UMAT), user-defined heat transfer (UMATHT) and user-defined expansion (UEXPAN) subroutines. In addition to these, another subroutine called URDFIL was used to access the results instantaneously during the analysis as required for realising the real-time coupling between deformation and mass diffusion. During the simulation process, the information was exchanged among the subroutines using common blocks. As the development was based on commercially available software, various loading conditions and model geometries could be fulfilled easily. The approach was extended to construct a failure line in terms of oxygen concentration and accumulated inelastic strain near the crack tip. The crack growth rates in oxidation environment can be predicted from the fatigue-oxidation failure line, although collecting physical evidence of crack-tip oxygen diffusion and experimental measurements of oxygen concentration near the crack tip are very challenging tasks and yet to be fulfilled.

Appendix A

In order to compute the pressure gradient, the inverse of Jacobian matrix is needed. For four-node quadrilateral elements, the four shape functions are:

$$N_i = \{(1-\xi)(1-\eta),(1+\xi)(1-\eta),(1+\xi)(1+\eta),(1-\xi)(1+\eta)\}/4,$$

where $i = 4$. Here, the shape functions of a quadrilateral element are expressed in terms of the local coordinates ξ and η. The derivative of the shape function with respect to local coordinates are obtained by:

$$\frac{dN_i}{d\xi} = \{-(1-\eta),(1-\eta),(1+\eta),-(1+\eta)\}/4,$$

$$\frac{dN_i}{d\eta} = \{-(1-\xi),-(1+\xi),(1+\xi),(1-\xi)\}/4.$$

The following relations were used to obtain the independent coordinates x and y:

$$x = \sum_{i=1}^{4} x_i N_i \quad y = \sum_{i=1}^{4} y_i N_i,$$

where x_i and y_i are the coordinates of the four nodes. Differentiating x and y with respect to the local coordinates ξ and η gives:

$$\frac{\partial x}{\partial \xi} = \sum_{i=1}^{4} x_i \frac{\partial N_i}{\partial \xi} \quad \frac{\partial x}{\partial \eta} = \sum_{i=1}^{4} x_i \frac{\partial N_i}{\partial \eta} \quad \frac{\partial y}{\partial \xi} = \sum_{i=1}^{4} y_i \frac{\partial N_i}{\partial \xi} \quad \frac{\partial y}{\partial \eta} = \sum_{i=1}^{4} y_i \frac{\partial N_i}{\partial \eta}.$$

The above can be written in matrix form as:

$$J = \begin{bmatrix} J_{11} & J_{12} \\ J_{21} & J_{22} \end{bmatrix} = \begin{bmatrix} \frac{\partial x}{\partial \xi} & \frac{\partial y}{\partial \xi} \\ \frac{\partial y}{\partial \eta} & \frac{\partial y}{\partial \eta} \end{bmatrix}$$

where J denotes Jacobian matrix. The inverse Jacobian matrix (J^{-1}) is then obtained by numerically inverting the J matrix.

Appendix B. Supplementary material

Supplementary data associated with this article can be found, in the online version, at http://dx.doi.org/10.1016/j.tafmec.2017.10.010.

References

[1] Johnston I A 2005 Understanding and predicting gun barrel erosion. Department of Defence, Defence Science and Technology Organisation, Australian Government, DSTO-R-757.

[2] A.G. Lichtenstein, The silver bridge collapse recounted, J. Perform. Constr. Facilit. 7 (1993) 249–261.

[3] A. Villani, E.P. Busso, K. Ammar, S. Forest, M.G.D. Geers, A fully coupled diffu- sional-mechanical formulation: numerical implementation, analytical validation, and effects of plasticity on equilibrium, Arch. Appl. Mech. 84 (2014) 1647–1664.

[4] R.H. Bricknell, D.A. Woodford, The mechanism of cavity formation during high temperature oxidation of nickel, Acta Metall. 30 (1982) 257–264.

[5] G. Calvarin-Amiri, A.M. Huntz, R. Molins, Effect of an applied stress on the growth kinetics of oxide scales formed on Ni-20Cr alloys, J. Mater. High Temp. 18 (2001) 91–99.

[6] V. Garat, O. Brucelle, J.M. Cloue, V. Rebeyrolle, D. Monceau, B. Viguier, E. Andrieu, Comparing different methods to determine the intergranular oxidation damage on a nickel based superalloy, Mater. Sci. Forum 461–464 (2004) 537–544.

[7] P. Sofronis, R.M. McMeeking, Numerical analysis of hydrogen transport near a bunting crack tip, J. Mech. Phys. Solids 37 (1989) 317–350.

[8] G. Mulin, P. Arevalo, A. Salleo, Influence of external mechanical loadings (creep, fatigue) on oxygen diffusion during nickel oxidation, Oxidat. Met. 45 (1994) 153–181.

[9] P. Berger, G. Moulin, M. Viennot, Nuclear microprobe study of stress-oxidation of nickel, Nucl. Instrum. Methods Phys. Res., Sect. B 130 (1997) 717–721.

[10] J.A. Pfaendtner, C.J. McMahon Jr., Oxygen-induced intergranular cracking of a Ni- base alloy at elevated temperatures – an example of dynamic embrittlement, Acta Mater. 49 (2001) 3369–3377.

[11] U. Krupp, W.M. Kane, C. Laird, C.J. McMahon Jr., Brittle intergranular fracture of a Ni-base superalloy at high temperatures by dynamic embrittlement, Mater. Sci. Eng. A 387–389 (2004) 409–413.

[12] U. Krupp, Dynamic embrittlement – time-dependent quasi-brittle intergranular fracture at high temperatures, Int. Mater. Rev. 50 (2005) 83–97.

[13] L.G. Zhao, Modeling of oxygen diffusion along grain boundaries in a nickel-based superalloy, J. Eng. Mater. Technol. 133 (2011) 031002.

[14] A. Karabela, L.G. Zhao, B. Lin, J. Tong, M.C. Hardy, Oxygen diffusion and crack growth for a nickel-based superalloy under fatigue-oxidation conditions, Mater. Sci. Eng. A 567 (2013) 46–57.

[15] J.P. Thomas, C.E. Chopin, Modeling of coupled deformation–diffusion in non- porous solids, Int. J. Eng. Sci. 37 (1999) 1–24.

[16] S. Prussin, Generation and distribution of dislocations by solute diffusion, J. Appl. Phys. 32 (1960) 1876–1881.

[17] N. Swaminathan, J. Qu, Y. Sun, An electrochemomechanical theory of defects in ionic solids: I Theory, Philos. Mag. 87 (2007) 1705–1721.

[18] J. Zhang, X. Zhao, Z. Suo, H. Jiang, A finite element method for transient analysis of concurrent large deformation and mass transport in gels, J. Appl. Phys. 105 (2009) 093522.

[19] M.J. Klein, The early papers of J. Willard Gibbs: a transformation of thermo- dynamics, in: E.G. Forbes (Ed.), Human Implications of Scientific Advance: Proceedings of the XVth International Congress of the History of Science, Edinburgh, 10–15 August 1977, edited by E.G. Forbes. Edinburgh University Press, Edinburgh, pp. 330–341.

[20] Y. An, H. Jiang, A finite element simulation on transient large deformation and mass diffusion in electrodes for lithium ion batteries, Modell. Simul. Mater. Sci. Eng. 21 (2013) 074007.

[21] R.J. Asaro, Micromechanics of crystals and polycrystals, Adv. Appl. Mech. 23 (1983) 1–115.

[22] E.P. Busso, Cyclic deformation of monocrystalline nickel alluminide and high temperature coatings, Massachusetts Institute of Technology, USA, 1990 PhD dis- sertation.

[23] R.J. Dennis, Mechanistic modelling of deformation and void growth behaviour in super-alloy single crystals, Imperial College London, UK, 2000 PhD dissertation.

[24] F.T. Meissonnier, E.P. Busso, N.P. O'Dowd, Finite element implementation of a genera-lised non-local rate-dependent crystallographic formulation for finite strains, Int. J. Plasticity 17 (2001) 601–640.

[25] ABAQUS, Version 6.11, Dassault Systemes Simulia Corp., Providence, USA, 2011.

[26] G.B. Stephenson, Deformation during interdiffusion, Acta Metall. 36 (1988) 2663–2683.

[27] A.T. Yokobori Jr., Y. Chinda, T. Nemoto, K. Satoh, T. Yamada, The effect of hy- drogen diffusion behavior on the embrittlement of steel under hydrogen atmo- spheric condition, Corros. Sci. 44 (2002) 407–424.

[28] S. Yoon, B. Han, On moisture diffusion modeling using thermal-moisture analogy, J. Electron. Packag. 129 (2007) 421–426.

[29] O. Aslan, Numerical modelling of hydrogen diffusion in metals accounting for large deformation, Int. J. Hydrogen Energy 40 (2015) 15227–15235.

[30] Z. Suo, D.V. Kubair, A.G. Evans, D.R. Clarke, V.K. Tolpygo, Stresses induced in alloys by selective oxidation, Acta Mater. 51 (2003) 959–974.

[31] H. Sehitoglu, W. Sun, The significance of crack closure under high temperature fatigue crack growth with hold periods, Eng. Fract. Mech. 33 (1989) 371–388.

[32] H.E. Evans, H.Y. Li, P. Bowen, A mechanism for stress-aided grain boundary oxi- dation ahead of cracks, Scripta Mater. 69 (2013) 179–182.